Journal of Inorganic and General Chemistry
ZAAC
Zeitschrift für anorganische und allgemeine Chemie
www.zaac.wiley-vch.de
RESEARCH ARTICLE

DOI: 10.1002/zaac.202500021

$Sm_2Ru_3Sn_5$: A Noncentrosymmetric Cubic Member of the $Ln_2M_3X_5$ Family

W. Kice Brown, Benny C. Schundelmier, Hengxin Tan, Corey Melnick, Gabriel Kotliar, Binghai Yan, Kaya Wei, Gregory T. McCandless, and Julia Y. Chan*

Dedicated to Dr. Gordon J. Miller on the occasion of his 65th birthday, in honor of his use of theoretical modeling and experimental investigation to advance the field of intermetallic compounds

An optimized synthetic method is presented for $Sm_2Ru_3Sn_5$ and investigate its physical properties and electronic structure. $Sm_2Ru_3Sn_5$ is prepared by arc-melting stoichiometric ratios of the elements and is confirmed by single crystal and powder X-ray diffraction. An antiferromagnetic transition is observed at $T_N = 3.8$ K. A modified Curie-Weiss fit to the data in the range 50–150 K yields a Curie-Weiss temperature: $\theta_{CW} = -36.6$ K and an effective magnetic moment: $\mu_{eff} = 0.83\,\mu_B$, in agreement with a Sm^{3+} oxidation state. Field-dependent magnetization up to H = 7 T at 2 K shows a maximum response of $0.06\,\mu_B$, which is significantly lower than the expected Sm^{3+} saturation moment ($0.71\,\mu_B$). Resistivity measurements indicate metallic behavior, and analysis of the magnetic entropy from the heat capacity reveals a doublet ground state due to crystal electric field splitting. The electronic structure and density of states are calculated with density function theory and further supported by the local density approximation with dynamical mean-field theory. The experimental and computational results highlight localized Sm^{3+} moments and suggest a possible interplay between Ruddelman–Kitel–Kasuya–Yosida and Kondo interactions, positioning $Sm_2Ru_3Sn_5$ as a promising material for studying topology and complex physical phenomena.

1. Introduction

Intermetallics compounds that contain samarium typically adopt trivalent or intermediate valent Sm oxidation states. Notable properties of Sm^{3+} compounds include the Kondo effect in $SmSn_3$,[1] heavy fermion behavior in Sm_3Te_4,[2] large magnetoresistance of over 100% at H = 9 T for $SmPd_2Ga_2$,[3] and multiple magnetic transitions are observed in Sm_2Sn_3.[4] A subset of Sm compounds is also recognized for their topology, where spin–orbit coupling (SOC) and *d–f* orbital hybridization can lead to nontrivial topological surface states. In SmB_6, the combination of topology and SOC creates a strong spin–orbit torque without exclusive surface conduction, a property that is intrinsic to topological insulators.[5,6] Another example is SmS that exhibits a pressure-induced valence instability, fluctuating from a Sm^{2+} to a Sm^{3+} state at 6.5 kbar.[7] The change in valence is accompanied by a first-order phase transformation, where the high-pressure golden phase (*g*-SmS) has a topological band structure containing Dirac cones.[8] $SmCoIn_5$ is another example of an intermediate-valent compound, where antiferromagnetic ordering dominates and Kondo coherence is not observed; however, charge fluctuations from the crystal field highlight a competition between Kondo and Ruderman–Kittel–Kasuya–Yosida (RKKY) interactions.[9] Finally, a large topological Hall effect was observed in the Weyl semimetal SmAlSi, which can be varied with magnetic field, supporting a Weyl-mediated, spiral magnetic ordering.[10] Our interest in finding a compound with high symmetry, topology, and SOC was influenced by the aforementioned examples.

In our 2023 survey of the $Ln_2M_3X_5$ compounds (Ln = lanthanide, or actinide; M = transition metal; X = Si, Ga, Ge, In, Sn), eight different structure types were identified.[11] Recently, $Ce_2Au_3In_5$ was identified as a Weyl–Kondo semimetal.[12] The authors predicted a number of strongly correlated topological semimetals and experimentally validated $Ce_2Au_3In_5$ (space group #31, $Pmn2_1$). Of the $Ln_2M_3X_5$ family of compounds, consisting of over 230 analogs, at least 15 examples are reported to have polymorphism or structural phase transformations, particularly the analogs with Groups 8 and 9 transition metals. Our group has studied $Pr_2Co_3Ge_5$ that exhibits valence instability from nearly

W. K. Brown, G. T. McCandless, J. Y. Chan
Department of Chemistry and Biochemistry, Baylor University, Waco, TX 70706, USA
E-mail: Julia_Chan@baylor.edu
B. C. Schundelmier, K. Wei
National High Magnetic Field Laboratory, Florida State University, Tallahassee, FL 32306, USA
B. C. Schundelmier
Department of Physics, Florida State University, Tallahassee, FL 32306, USA
H. Tan, B. Yan
Department of Condensed Matter Physics, Weizmann Institute of Science, Rehovot 7610001, Israel
C. Melnick, G. Kotliar
Department of Physics and Astronomy, Rutgers University, Piscataway, NJ 08854, USA
C. Melnick, G. Kotliar
Department of Matter Physics and Materials Science, Brookhaven National Laboratory, Upton, NY 11973, USA

Supporting information for this article is available on the WWW under https://doi.org/10.1002/zaac.202500021

Pr^{4+} to Pr^{3+} upon a monoclinic to orthorhombic structural phase transition.[13] Another notable $Ln_2M_3X_5$ analog is polymorphic $Sm_2Ru_3Ge_5$ that adopts both the tetragonal $Sc_2Fe_3Si_5$ and the orthorhombic $U_2Co_3Si_5$ structure types,[14,15] where each polymorph has been linked to charge density wave behavior.[15,16] While both polymorphs exhibit Sm^{3+} character, the magnetism of each manifests differently. The tetragonal polymorph exhibits a ferromagnetic transition at 7 K;[15] however, the orthorhombic polymorph of $Sm_2Ru_3Ge_5$ has an antiferromagnetic transition at 7 K.[17] Sm-containing compounds, particularly those adopting the $Ln_2M_3X_5$ structures, offer a rich system to study complex structural and magnetic phenomena. For these reasons, $Sm_2Ru_3Sn_5$ was chosen to be the focus of this study as a potential candidate for strongly correlated phenomena. While quite different from the other $Ln_2M_3X_5$ structure types, $Sm_2Ru_3Sn_5$ ($a = 9.4606(8)$ Å; $I\bar{4}3m$)[18] adopts a structure that is a noncentrosymmetric variation from the binary cubic, centrosymmetric Ru_3Sn_7 structure ($a = 9.332$ Å; $Im\bar{3}m$).[19] Since a topological band structure has been established for Ru_3Sn_7 analogs,[20] an investigation into the noncentrosymmetric analog could reveal new states that were unrealized in the centrosymmetric environment. Furthermore, there is no understanding on the impact of *f*-elements to physical properties of the Ru_3Sn_7 structure type. Herein, we report an investigation of the synthesis, physical properties, and electronic structure of $Sm_2Ru_3Sn_5$ to understand the introduction of *f*-orbitals to the Ru_3Sn_7 structure type.

2. Results and Discussion

2.1. Synthesis

A previous synthesis of $Sm_2Ru_3Sn_5$ arc-melted and annealed samples at 600 °C for 30 days, where Ru and $SmRuSn_3$ impurities were observed in 15 wt% and 5 wt%, respectively.[18] Single crystals suitable for X-ray diffraction were isolated from the surface of the annealed samples. Similarly, we also synthesized $Sm_2Ru_3Sn_5$ by arc-melting stoichiometric amounts of Sm, Ru, and Sn. Annealing seemed to have no impact on the formation of $Sm_2Ru_3Sn_5$; however, an important experimental condition to the formation of $Sm_2Ru_3Sn_5$ was the particle size of Ru used in the experiment. Larger pieces of Ru introduced inhomogeneous regions to the boule, resulting in areas of different stoichiometry that contributed to the formation of byproducts. Ru powder was vital for consistent formation of $Sm_2Ru_3Sn_5$ without any by-products. A small homogeneity range of formation was observed, and any deviation in stoichiometry from the 2:3:5 (Sm:Ru:Sn) ratio results in the formation of Ru_2Sn_3 and $SmRuSn_3$ as impurities. Prior to arc-melting, the Ru powder was mixed with the pieces of Sm and Sn and pressed into a pellet to ensure a homogeneous reaction environment. Attempts to grow single crystals with the flux method from excess Sn led to the formation of Ru_3Sn_7 and $SmRuSn_3$, excess Ga or In flux led to the formation of both RuX_3 and SmX_2 (X = Ga, In), and excess Bi flux led to the formation of Ru_3Sn_7 and Ru_2Sn_3.

2.2. Crystal Structure

$Sm_2Ru_3Sn_5$ crystallizes in the cubic space group $I\bar{4}3m$ (No. 217) with room temperature unit cell parameter: $a = 9.4575(5)$ Å. Details of the single crystal data collection and refinement parameters are outlined in **Table 1**. $Sm_2Ru_3Sn_5$ is an ordered noncentrosymmetric variant of the centrosymmetric Ru_3Sn_7 structure, consistent with the previously reported lattice parameter $a = 9.4606(8)$ Å.[18] The Ru_3Sn_7 structure can be visualized as a collection of doubled, condensed square antiprisms that form interpenetrating frameworks (**Figure 1**a), consisting of three atomic positions: Ru1 (12*e*, 4 *m* . *m*), Sn1 (12*d*, $\bar{4}$ *m* . 2), and Sn2 (16*f*, . 3 *m*).[21,22] The doubled square antiprisms of Ru_3Sn_7 are connected by a Sn_8 cube with the Sn2 site at the vertices. To compare the Sn2 sites to the structure of $Sm_2Ru_3Sn_5$, the cube can also be described as two congruent, interpenetrating tetrahedra (Figure 1b). The crystal structure of $Sm_2Ru_3Sn_5$ consists of four atomic positions: Sm1 (8*c*, 3 *m*), Ru1 (12*e*, 2 . *m m*), Sn1 (12*d*, $\bar{4}$), and Sn2 (8*c*, . 3 *m*), where the fractional atomic coordinates are outlined in **Table 2**. In $Sm_2Ru_3Sn_5$, the tetrahedra are incongruent—one made from four Sn2 atoms and one made from four Sm1 atoms. This motif of two, interpenetrating Ln_4 and Sn_4 tetrahedra (Figure 1c), is also present in the $Ho_5Co_6Sn_{18}$, where the Ho tetrahedral sublattice is associated with geometric frustration, and the spins order noncollinearly.[23] While the distance between the Sm atoms in $Sm_2Ru_3Sn_5$ is too far to be considered within bonding distance ($d_{Sm-Sm} = 5.373(1)$ Å), it is comparable to the interatomic distance in the $Ho(2)_4$ tetrahedron ($d_{Ho-Ho} = 5.06$–5.15 Å) for $Ho_5Co_6Sn_{18}$.

Electron counting has been discussed in relation to the Ru_3Sn_7 structure type as a way to rationalize the chemical composition of substituted analogs.[21,24,25] For $Sm_2Ru_3Sn_5$ and Ru_3Sn_7, the valence electron concentrations (VEC) are 50 (5 e^- $atom^{-1}$) and 52 (5.2 e^- $atom^{-1}$), respectively. While VEC is a useful tool to identify trends within a given structure type or class of intermetallics, normalization of VEC to the transition metal sites offers insight into the bonding.[25] In the case of Ru_3Sn_7, there are 52

Table 1. Single crystal data collection and refinement parameters for $Sm_2Ru_3Sn_5$.

Formula	$Sm_2Ru_3Sn_5$	
Space Group	$I\bar{4}3m$	
Temperature [K]	298	160
a [Å]	9.4575(5)	9.4438(6)
V [Å^3]	845.92(13)	842.25(16)
Z	4	
θ [°]	3.1–30.5	
μ [mm^{-1}]	33.23	33.37
Measured Reflections	19123	21240
Independent Reflections	272	272
R_{int}	0.073	0.082
$\Delta\varrho_{max}$, $\Delta\varrho_{min}$ [e$^-$ Å^{-3}]	0.57, −0.62	0.89, −1.11
R [$F^2 > 2\sigma(F^2)$]	0.011	0.015
wR_2 (F^2)	0.024	0.030
$R = \sum \lvert\lvert F_o\rvert - \lvert F_c\rvert\rvert / \sum \lvert F_o\rvert$		
$wR_2 = (\sum[[w(F_o^2 - F_c^2)^2] / \sum[w(F_o^2)^2]])^{1/2}$		

Journal of Inorganic and General Chemistry
ZAAC
Zeitschrift für anorganische und allgemeine Chemie

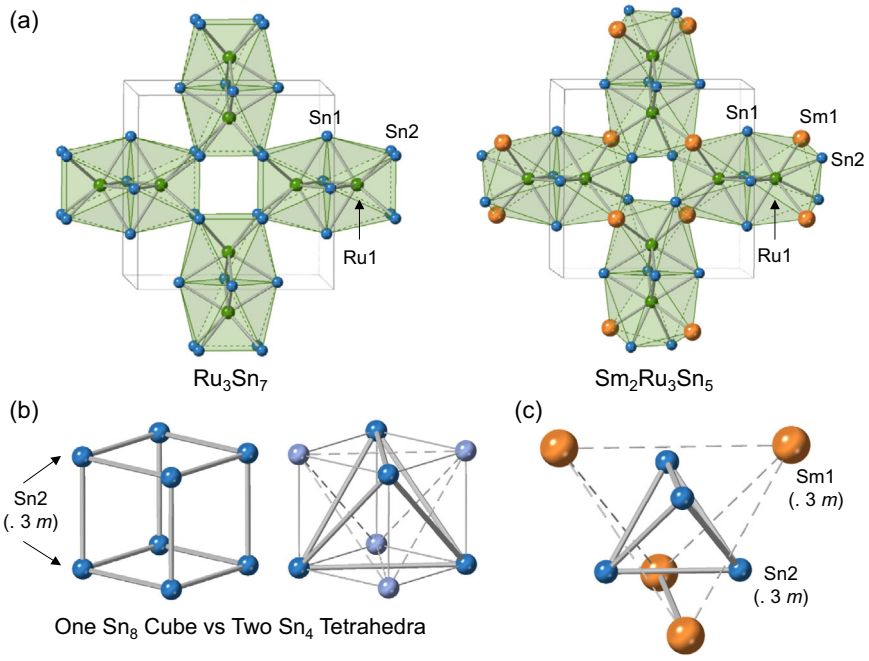

Figure 1. a) Views of the face-sharing square antiprisms (Ru_3Sn_7) and distorted 8-vertex polyhedra ($Sm_2Ru_3Sn_5$). b) Sn2 (16*f*) atomic sites in Ru_3Sn_7 can be visualized as either one Sn_8 cube or two Sn_4 Tetrahedra. c) Sm1 (8*c*) and Sn2 (8*c*) atomic sites in $Sm_2Ru_3Sn_5$ that form two incongruent tetrahedra.

Table 2. Fractional atomic coordinates and displacement parameters (T = 298 K).

Site	Wyckoff	*x*	*y*	*Z*	U_{eq} [Å^2]
Sm	8*c*	0.20088(4)	*x*	*X*	0.01085(15)
Ru	12*e*	1/2	0.14990(8)	1/2	0.00727(16)
Sn1	12*d*	1/4	0	1/2	0.00986(15)
Sn2	8*c*	0.38416(6)	*x*	*X*	0.00776(17)

valence electrons (8 electrons from each of the 3 Ru atoms and 4 electrons from each of the 7 Sn atoms). When normalized to the transition metal, there are 17.33 electrons/Ru that can be rationalized with the 18-$n + m$ rule.[26] Assuming Sm^{3+}, the VEC drops to 16.67 electrons/Ru in $Sm_2Ru_3Sn_5$. The reduced VEC implies either an increase in the Ru—Ru bonding within the structure (the *n* term) or a reduced Sn—Sn interaction (the *m* term). A change in the degree of Ru—Ru bonding can be ruled out, since there is a minimal contraction of 0.064(2) Å for the Ru—Ru contacts in $Sm_2Ru_3Sn_5$ (compared to Ru_3Sn_7). Coupled with this change (shown in Figure 1) is a similar amount of expansion in the Sn2—Sn2 connectivity due to the replacement of half the Sn2 atoms (3 *m* site symmetry) in the Ru_3Sn_7 structure with Sm ($Sm_2Ru_3Sn_5$: $d_{tet} = 3.100(6)$ Å; Ru_3Sn_7: $d_{cube} = 3.020(1)$ Å). It is possible that the change in the *m* term is more heavily influenced by the introduction of Sm—Sn interactions ($d_{Sm1-Sn2} = 3.004(5)$ Å) between adjacent tetrahedra; however, deviations from the ideal VEC could also be explained by a high density of states (DOS) at the Fermi level. To further understand the impact of this structural distortion on the chemistry of $Sm_2Ru_3Sn_5$, we investigated the physical properties and electronic structure.

2.3. Physical Properties

Figure 2 shows the magnetic susceptibility and field-dependent magnetization measurements of $Sm_2Ru_3Sn_5$. An antiferromagnetic transition at $T_N = 3.8$ K is observed (shown in Figure 2a). The inverse susceptibility (Figure 2b) shows a slight curvature that is consistent with a temperature independent magnetic term. The magnetic susceptibility data were fit from 50 to 150 K with a modified Curie-Weiss law: $\chi = \chi_0 + C/(T - \theta_{CW})$, where the temperature-independent term: $\chi_0 = 0.0026$, *C* is the Curie constant, and the Curie-Weiss temperature: $\theta_{CW} = -36.6$ K. The effective moment from the fit was 0.83 μ_B, consistent with the expected effective moment for Sm^{3+} ($\mu_{eff} = 0.84\,\mu_B$). The modified Curie-Weiss law fits the magnetic data more accurately by introducing a constant accounting for temperature-independent contributions to the data; however, the discrepancy between T_N and θ_{CW} implies contributions from at least one of three possible explanations. 1) Sm commonly exhibits van Vleck paramagnetic contributions to its magnetism. This arises from population of both the $J = 5/2$ ground state and the $J = 7/2$ excited states. 2) While $Sm_2Ru_3Sn_5$ is cubic, directional dependence of interactions (anisotropy) can also cause frustration. Considering the frustration index ($f = \theta_{CW}/T_N$), $Sm_2Ru_3Sn_5$ has a value: $f = 9.6$. Even though a value of $f > 5$ is accepted for frustrated 3*d* transition metal magnets, similar values for 4*f* magnets should be treated with caution as the θ_{CW} may be potentially inflated due to crystal field effects.[27,28] $SmPd_2Al_3$ is a compound with a strongly anisotropic magnetic response.[29] Subsequent magnetometry and neutron diffraction experiments illuminated a geometrically frustrated Sm lattice with complex magnetic behavior that is influenced

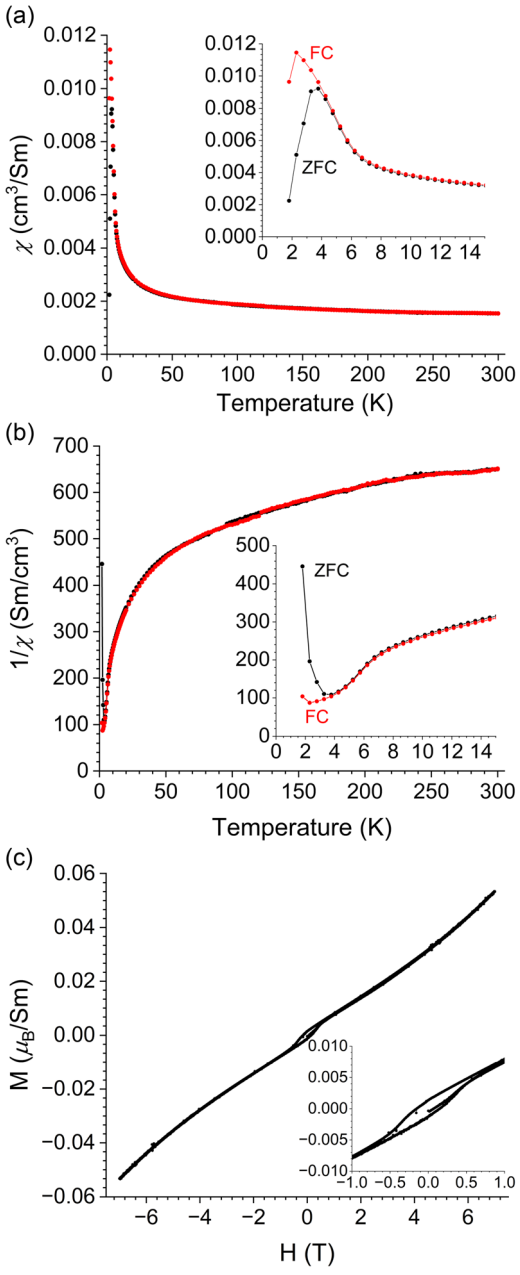

Figure 2. a) The magnetic susceptibility for polycrystalline $Sm_2Ru_3Sn_5$ at H = 0.1 T. Inset shows the low temperature transition. The red points represent the field cooled (FC) experiment, and the black points represent the zero field cooled (ZFC) experiment. b) The inverse of the magnetic susceptibility of $Sm_2Ru_3Sn_5$. c) The field-dependent magnetization for $Sm_2Ru_3Sn_5$ measured at T = 2 K.

by the kinetic effect of a sweeping magnetic field.[30] 3) The large difference between θ_{CW} and T_N could also arise from Sm moments being screened by the conduction electrons. The phenomenon could be mediated by RKKY[31,32] or Kondo interactions.[33,34] In systems with strong spin–orbit coupling (SOC), the preferred alignment directions of spins can conflict with each other, causing the original Curie-Weiss law to break down from temperature-dependent local magnetic moments.[35] A combination of SOC and frustration could lead to fractionalization of fermionic excitations, known as a quantum spin liquid.[36] These findings indicate $Sm_2Ru_3Sn_5$ may be a good candidate to study low-temperature Kondo screening in a cubic, noncentrosymmetric environment. The MvH measurements (Figure 2c) were collected below the antiferromagnetic transition at 2 K and show a slight hysteresis at low fields as well as a small, field-dependent response; however, no saturation was observed up to 7 T with a response that is an order of magnitude lower than the calculated saturation moment (0.71 μ_B).

The resistivity of $Sm_2Ru_3Sn_5$ is shown in **Figure 3**a. The measured compound is metallic and has a slight curvature, similar to the shape of the resistivity for Ru_3Sn_7.[37] The authors report the nonlinearity of the resistivity in Ru_3Sn_7 to be similar to the A15 (Nb_3Sn) compounds and relate the curvature to the presence of *d*-orbitals near the Fermi level. The resistivity $Sm_2Ru_3Sn_5$ at room temperature (≈200 $\mu\Omega$-cm) is nearly three times that of the reported value for Ru_3Sn_7 at room temperature (≈70 $\mu\Omega$-cm). It is worth noting the impact of Sb-doping on the resistivity of Ru_3Sn_7.[38] $Ru_3Sb_{1.75}Sn_{5.25}$ has a similar room temperature resistivity value (≈250 $\mu\Omega$-cm); however, it also superconducts at 4.1 K. This phenomenon is attributed it to local maxima near the Fermi level in the DOS.

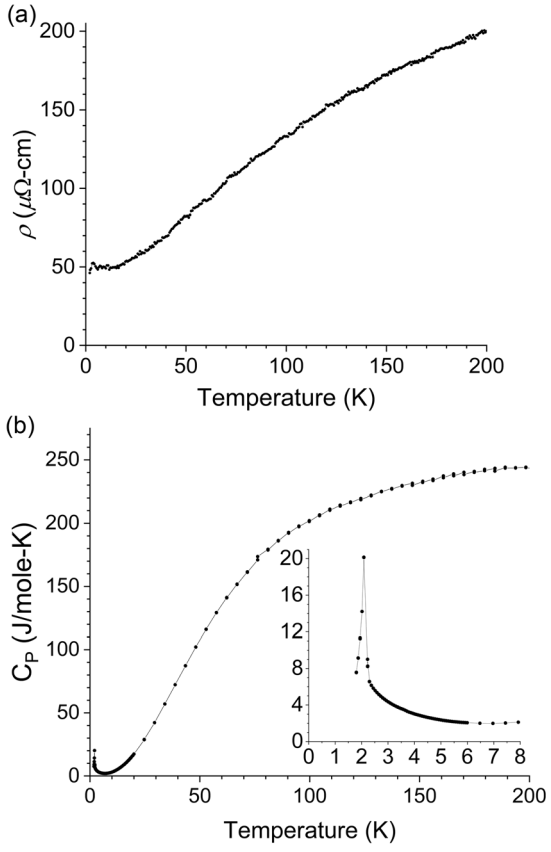

Figure 3. a) Temperature-dependent electrical resistivity of a polished piece of polycrystalline $Sm_2Ru_3Sn_5$ measured using a four-point probe method. b) Temperature-dependent heat capacity for $Sm_2Ru_3Sn_5$ measured on the same sample. Inset shows a sharp feature at 2.1 K, consistent with the antiferromagnetic transition.

The heat capacity of $Sm_2Ru_3Sn_5$ is shown in Figure 3b. There is a sharp peak at 2.1 K, consistent with the antiferromagnetic transition from field cooled magnetic susceptibility measurement ($T_N = 2.3$ K). The data were fit with a Lattice-Debye model. After subtraction of the lattice contribution, the magnetic contribution to the heat capacity (C_{mag}) was integrated to find the magnetic entropy (S_{mag}). The magnetic entropy saturates at a value of R ln 2, consistent with a doublet ground state for the measured temperature range. This is lower than a full $J = 5/2$ expected for a Sm^{3+} compound. A saturation of the magnetic entropy is observed for other Sm^{3+} compounds and is often attributed to crystal electric field effects caused by splitting of the f states.[29,39,40]

2.4. Electronic Structure

Figure 4 shows the band structure and DOS for Ru_3Sn_7 and $Sm_2Ru_3Sn_5$ calculated with density functional theory (DFT). Both materials are metals, in agreement with the measured resistivity. The DOS near the Fermi energy of both materials is mainly composed of Ru d and Sn p orbitals, while the Sm atoms contribute little to the DOS of $Sm_2Ru_3Sn_5$. In addition to the metallic behavior, both materials possess rich topological properties, as evidenced by multiple band crossings in their electronic structures when spin–orbit coupling (SOC) is not included. Due to their high crystalline symmetry—$Im\bar{3}m$ (No. 229) for Ru_3Sn_7 and $I\bar{4}3m$ (No. 217) for $Sm_2Ru_3Sn_5$—Dirac nodal lines are expected to emerge along certain high-symmetry k-paths. However, these band crossings become gapped once SOC is considered. Notably, $Sm_2Ru_3Sn_5$, which lacks inversion symmetry, hosts Rashba-type SOC, whereas Ru_3Sn_7, which preserves inversion symmetry, does not (Figure 4). This contrast makes these two materials ideal platforms for exploring how elemental substitution influences different types of SOC effects, particularly in these intriguing topological systems.

The local density approximation with dynamical mean-field theory (LDA + DMFT) calculations support the localized picture (Sm^{3+}) of the f electrons in the measured range of temperatures. **Figure 5**a displays the local DOS at $T = 600$ K, and the total DOS. The f electrons are in a Mott state with fluctuating local moments and no weight at the Fermi level: The local DOS of the f electrons displays Hubbard bands in the one electron spectra. Figure 5b displays the probability distribution of the electronic configurations with different numbers of f electrons. The dominant occupation is Sm^{3+} with N = 5 electrons, an open shell with a local fluctuating moment. In this material, the conduction electrons are scattered by the local moments, and this additional scattering channel provides a possible explanation for the much larger value

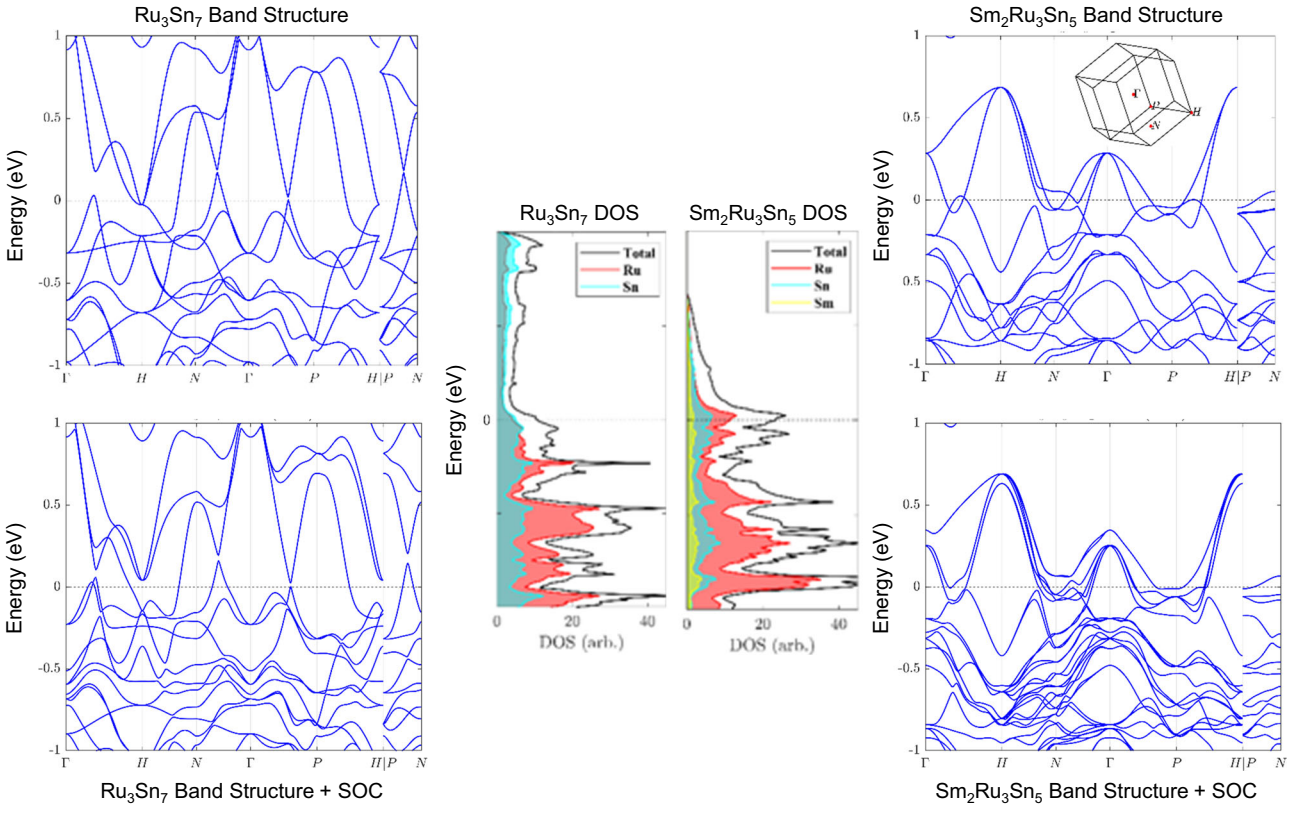

Figure 4. Band structure and density of state (DOS) of Ru_3Sn_7 (left) and $Sm_2Ru_3Sn_5$ (right), with the DOS plots (center). High-symmetry points in the Brillouin zone are shown in the inset of the $Sm_2Ru_3Sn_5$ band structure panel. In the DOS plots, both the total and element-resolved DOSs are shown. The charge neutral point (Fermi energy) is set to zero energy. Band structures of the two materials with spin–orbit coupling (SOC) are shown later. The band crossings are gapped out by SOC in both materials. The Rashba-type SOC is present in $Sm_2Ru_3Sn_5$ but not in Ru_3Sn_7.

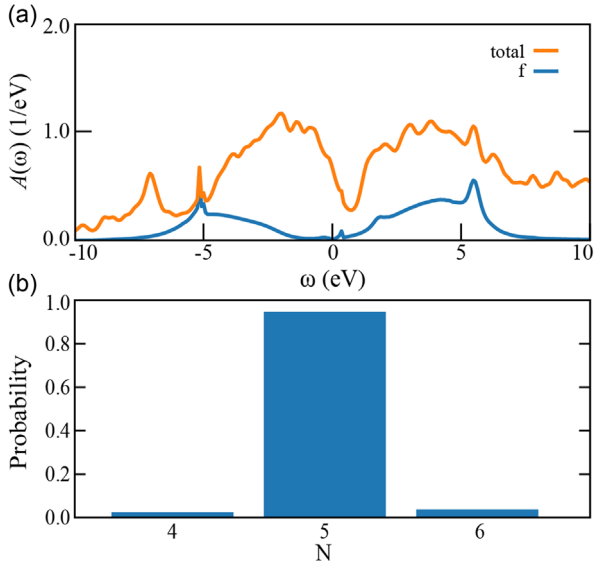

Figure 5. Spectral functions and valence histogram in $Sm_2Ru_3Sn_5$ as predicted within one-shot LDA + DMFT at $T = 600$ K. There is no Sm-*f* character on the Fermi surface, and the valence is almost always in the $N = 5$ sector.

of the high-temperature resistivity of $Sm_2Ru_3Sn_5$ relative to Ru_3Sn_7. These local moments can be partially Kondo screened at lower temperatures, as it has been observed, for example, in UGe_2.[41] This could account for the reduced magnetic entropy observed in the heat capacity (Figure 3). In this picture, one can interpret the scale of $\theta_{CW} = -36.6$ K extracted from the susceptibility as a Kondo scale. Indeed, there are clear differences between the DFT and DFT + DMFT electronic structure. Correlations remove *f* spectral weight from the fermi level, and this is expected in such a correlated material containing open shell elements from the 4*f* series. It would be very interesting to probe this using photoemission or scanning tunneling microscopy measurements.

3. Conclusions

We have successfully prepared $Sm_2Ru_3Sn_5$ and measured its physical properties. Our joint experimental and computational methods support localized Sm *f* electrons. An antiferromagnetic transition is observed at $T_N = 3.8$ K, and our DFT and LDA + DMFT calculations indicate a dominant Sm^{3+} occupation of the electronic configuration probability distribution. Based on the local DOS ($T = 600$ K), the *f*-electrons are in a Mott state indicating the presence of Hubbard bands. Notably, the θ_{CW} is an order of magnitude larger than the ordering temperature implying either van Vleck paramagnetic contributions to the magnetism, geometric frustration of the magnetic moments, or partial Kondo screening of the Sm magnetic moments at low temperatures. Our analysis of the heat capacity for $Sm_2Ru_3Sn_5$ is consistent with a doublet ground state, implying the presence of crystal field effects which could artificially inflate θ_{CW} and impact the frustration parameter. The geometric frustration could be explained by the tetrahedral Sm sublattice; however, other measurements indicate possible screening of the local Sm moments by the conduction electrons. The reduced moment of $\approx 0.06\,\mu_B$/Sm in $Sm_2Ru_3Sn_5$ can be attributed to partial screening of localized magnetic moments by conduction electrons. For comparison, $SmPd_2Al_3$ (where Sm also carries a Sm^{3+} moment) shows a lower than expected magnetic moment of $0.16\,\mu_B$/Sm due to strong crystal field effects.[30] Transport measurements of $Sm_2Ru_3Sn_5$ indicated a higher resistivity than Ru_3Sn_7. This could be explained by local Sm magnetic moments contributing to the scattering of the conduction electrons.

Given the interest in SmB_6 (a topological Kondo insulator) and $SmCoIn_5$ (an antiferromagnet with Kondo screening), low-temperature resistivity measurements to probe $Sm_2Ru_3Sn_5$ for a Kondo resonance would be very useful in confirming Kondo screening of the Sm moments in $Sm_2Ru_3Sn_5$. Our joint experimental and computational methods suggest the presence of Hubbard bands, making it worthwhile to explore the possibility of suppressing magnetism to observe a Kondo lattice. Given the nature of the magnetism, inelastic X-ray scattering measurements would also be useful in experimentally confirming the electronic structure or the Fermi surface of $Sm_2Ru_3Sn_5$. The competition between RKKY-type interactions and Kondo behavior opens exciting possibilities for studying topology and discovering new quantum materials to explore complex physical phenomena.

4. Experimental Section

$Sm_2Ru_3Sn_5$ was prepared via arc melting. Stoichiometric ratios of the elements were measured and pressed together in a hydraulic press to create a homogeneous environment and prevent Ru powder from coating the interior of the setup. The elements were melted into a single boule under a positive flow of Ar gas. A Zr "getter" was included in the reaction setup to minimize oxidation of the sample. The boule was flipped and remelted three times for homogeneity. Single crystals were isolated from a fragment of the arc-melted boule ($\approx 0.01 \times 0.01 \times 0.02$ mm) and used to collect X-ray diffraction data at $T = 160$ and 298 K (earlier and later the previously reported temperature of $T = 240$ K).[18] Data were collected using a Bruker D8 Quest Kappa single-crystal X-ray diffractometer equipped with an Incoatec IμS microfocus source (Mo K_α radiation, $\lambda = 0.71073$ Å) and a PHOTON III CPAD area detector. The raw frames were integrated with Bruker SAINT, and the intensities were corrected for absorption with a multi-scan method in SADABS.[42] The intrinsic phasing method in SHELXT was used to generate preliminary crystallographic models,[43] which were finalized with least-squares refinements in SHELXL.[44] The details of the data collection, refinement parameters, and atomic coordinates are described in Table 1 and 2.

Pieces of the arc-melted boule were also ground in an agate mortar and pestle. The powder was then placed on a low-background sample holder, and the powder X-ray diffraction data were collected on a Bruker D2 Phaser equipped with a Cu K_α source ($\lambda = 1.54184$ Å) and a LYNXEYE XE-T detector. Data were collected in the 2θ range 5–80° at room temperature and were analyzed by a Pawley fit in TOPAS (shown in Figure S1, Supporting Information).[45]

Energy-dispersive X-ray spectroscopy (EDS) was performed on a piece of the arc-melted boule with a VERSA 3D focused ion beam scanning electron microscope. The formula obtained from EDS was $Sm_{1.9(5)}Ru_{3.1(4)}Sn_{5.0(2)}$, in good agreement with the nominal composition.

Temperature-dependent magnetization data were collected on polycrystalline $Sm_2Ru_3Sn_5$ using a Quantum Design MPMS system. The sample was zero-field-cooled (ZFC), then measured on warming from 1.8 to 300 K in an external magnetic field of 0.1 T. The field-dependent magnetization data were collected at 1.8 K in a range −7–7 T. The electrical resistance and heat capacity were measured on the same sample in a Quantum Design PPMS system. For the electrical resistance, a standard 4-probe method was employed on the same sample, where each probe consisted of 0.002 in. diameter Pt wire attached with silver paste. A current of 500 μA was applied, and resistance was measured on cooling in the temperature range of 300–2 K. We observed no anomalies in the resistivity or decomposition of the sample that would be consistent with the formation of silver stannides.

The electronic structure was calculated using DFT as implemented in the Vienna *Ab-initio* Simulation Package.[46] The Perdew, Burke, and Ernzerhof generalized gradient approximation[47] was employed to model the electron exchange–correlation interactions for all elements. The projected augmented wave method[48] was utilized with 8 valence electrons for Ru, 4 for Sn and 11 for Sm (treating the Sm *f* electrons as core states). The valence electron configuration for Sm is $5s^2$–$5p^6$–$6s^2$–$5d^1$, resulting a 3+ valence for Sm. All crystal structures were fully relaxed until the forces on all atoms were below 1 meV Å^{-1}. A plane-wave basis set with an energy cutoff of 300 eV was used. The reciprocal space was sampled using a $10 \times 10 \times 10$ k-point mesh. Spin–orbit coupling was not included. The DOS was calculated using the tetrahedron method with Blöchl corrections.

To calculate the electronic structure including correlation effects, we used codes in Comsuite.[49] In particular, we conducted one-shot DFT + dynamical mean field theory (DFT+DMFT) calculations using *Portobello*,[50] the all-electron code FlapwMBPT[51,52,53] to solve the fully relativistic DFT problem within the local density approximation, and the continuous-time quantum Monte Carlo code ComCTQMC[52] to solve the quantum impurity problem. The Sm-4*f* shell is treated as correlated, and a spherically symmetric Slater–Condon interaction is applied with Hubbard interaction $U = 6.5$ eV and Hund interaction $J = 0.7$ eV. We use the nominal double counting[54] with nominal occupancy $N_0 = 5$ and conduct the calculations at 600 K. We then computed the spectral functions of the *f* electrons, $A(\omega)$, and the valence histogram, i.e., the projection of the many-body density matrix onto the number of electrons, *N*.

Accession Codes

Crystallographic data (excluding structure factors) for the structures reported in this article have been deposited with the Cambridge Crystallographic Data Centre as supplementary publication no. CSD-2421218–2421219. Copies of the data can be obtained free of charge on application to CCDC, 12 Union Road, Cambridge CB2 1EZ, UK [fax.: (internat.) + 441223/336-033; e-mail: deposit@ccdc.cam.ac.uk].

Acknowledgements

J.Y.C. gratefully acknowledges the support of both the Welch Foundation, AA-2056-20240404 and the U.S. Department of Energy, DE-SC0022854. A portion of this work was performed at the National High Magnetic Field Laboratory (NHMFL), which is supported by National Science Foundation Cooperative Agreement No. DMR-2128556 and the State of Florida. B.C.S., and K.W. acknowledges the support of the NHMFL User Collaboration Grant Program (UCGP). G.K. and C.M. were supported by the US Department of Energy, Office of Basic Energy Sciences as part of the Computation Material Science Program.

Conflict of Interest

The authors declare no conflict of interest.

Data Availability Statement

The data that support the findings of this study are available from the corresponding author upon reasonable request.

Keywords: intermetallic compounds · lanthanides · materials science · samarium · transition metals

[1] M. Kasaya, B. Liu, M. Sera, T. Kasuya, D. Endoh, T. Goto, T. Fujimura, *J. Magn. Magn. Mater.* **1985**, *52*, 289.
[2] U. Ahlheim, K. Fraas, P. H. P. Reinders, F. Steglich, O. Nakamura, T. Suzuki, T. Kasuya, *J. Magn. Magn. Mater.* **1992**, *108*, 213.
[3] W. M. Williams, R. T. Macaluso, M. Moldovan, D. P. Young, J. Y. Chan, *Inorg. Chem.* **2003**, *42*, 7315.
[4] M. L. Fornasini, P. Manfrinettib, A. Palenzonab, S. K. Dharc, *Z. Naturforsch., B: Chem. Sci.* **2003**, *58*, 521.
[5] M. Dzero, K. Sun, V. Galitski, P. Coleman, *Phys. Rev. Lett.* **2010**, *104*, 106408.
[6] Y. Li, Q. Ma, S. X. Huang, C. L. Chien, *Sci. Adv.* **2018**, *4*, eaap8294.
[7] C.-J. Kang, H. C. Choi, K. Kim, B. I. Min, *Phys. Rev. Lett.* **2015**, *114*, 166404.
[8] C.-J. Kang, D.-C. Ryu, J. Kim, K. Kim, J. S. Kang, J. D. Denlinger, G. Kotliar, B. I. Min, *Phys. Rev. Mater.* **2019**, *3*, 081201.
[9] D. W. Tam, N. Colonna, N. Kumar, C. Piamonteze, F. Alarab, V. N. Strocov, A. Cervellino, T. Fennell, D. J. Gawryluk, E. Pomjakushina, Y. Soh, M. Kenzelmann, *Commun. Phys.* **2023**, *6*, 223.
[10] X. Yao, J. Gaudet, R. Verma, D. E. Graf, H.-Y. Yang, F. Bahrami, R. Zhang, A. A. Aczel, S. Subedi, D. H. Torchinsky, J. Sun, A. Bansil, S.-M. Huang, B. Singh, P. Blaha, P. Nikolić, F. Tafti, *Phys. Rev. X* **2023**, *13*, 011035.
[11] W. K. Brown, M. A. Plata, M. E. Raines, J. Y. Chan, *Handbook on the Physics and Chemistry of Rare Earths*, (Eds: J.-C. G. Bunzli, S. M. Kauzlarich), Elsevier, Amsterdam **2023**, *64*, pp. 1–92.
[12] L. Chen, C. Setty, H. Hu, M. G. Vergniory, S. E. Grefe, L. Fischer, X. Yan, G. Eguchi, A. Prokofiev, S. Paschen, J. Cano, Q. Si, *Nat. Phys.* **2022**, *18*, 1341.
[13] T. M. Kyrk, E. R. Kennedy, J. Galeano-Cabral, G. T. McCandless, M. C. Scott, R. E. Baumbach, J. Y. Chan, *Sci. Adv.* **2024**, *10*, eadl2818.
[14] G. Venturini, M. Méot-Meyer, J. F. Marêché, B. Malaman, B. Roques, *Mater. Res. Bull.* **1986**, *21*, 33.
[15] D. E. Bugaris, C. D. Malliakas, F. Han, N. P. Calta, M. Sturza, M. J. Krogstad, R. Osborn, S. Rosenkranz, J. P. C. Ruff, G. Trimarchi, S. L. Bud'ko, M. Balasubramanian, D. Y. Chung, M. G. Kanatzidis, *J. Am. Chem. Soc.* **2017**, *139*, 4130.
[16] R. Sokkalingam, G. Lingannan, M. Sundaramoorthy, C. S. Lue, C. N. Kuo, B. Joseph, S. Arumugam, *Solid State Commun.* **2023**, *372*, 115293.
[17] C. N. Kuo, C. J. Hsu, C. W. Tseng, W. T. Chen, S. Y. Lin, W. Z. Liu, Y. K. Kuo, C. S. Lue, *Phys. Rev. B* **2020**, *101*, 155140.

[18] V. Pavlova, E. Murashova, *Z. Kristallogr. Cryst. Mater.* **2021**, *236*, 137.
[19] O. Nial, *Sven. Kem. Tidskr* **1947**, *59*, 172.
[20] A. Flessa Savvidou, A. Ptok, G. Sharma, B. Casas, J. K. Clark, V. M. Li, M. Shatruk, S. Tewari, L. Balicas, *npj Quantum Mater.* **2023**, *8*, 68.
[21] U. Häussermann, M. Elding-Pontén, C. Svensson, S. Lidin, *Chem. Eur. J.* **1998**, *4*, 1007.
[22] L. Eriksson, J. Lanner, *Acta Crystallogr. E.* **2001**, *57*, i85.
[23] C.-W. Wang, S. K. Karna, S.-i. Yano, C.-H. Lee, M. Avdeev, C. S. Lue, C. N. Kuo, *Phys. Rev. B* **2022**, *105*, 104429.
[24] D. Swenson, *MRS Online Proc. Libr.* **1996**, *453*, 367.
[25] V. J. Yannello, B. J. Kilduff, D. C. Fredrickson, *Inorg. Chem.* **2014**, *53*, 2730.
[26] V. J. Yannello, D. C. Fredrickson, *Inorg. Chem.* **2015**, *54*, 11385.
[27] A. P. Ramirez, *Annu. Rev. Mater. Res.* **1994**, *24*, 453.
[28] S. Mugiraneza, A. M. Hallas, *Commun. Phys.* **2022**, *5*, 95.
[29] J. Pospíšil, M. Kratochvílová, J. Prokleška, M. Diviš, V. Sechovský, *Phys. Rev. B* **2010**, *81*, 024413.
[30] J. Pospíšil, G. Nénert, S. Miyashita, H. Kitazawa, Y. Skourski, M. Diviš, J. Prokleška, V. Sechovský, *Phys. Rev. B* **2013**, *87*, 214405.
[31] M. A. Ruderman, C. Kittel, *Phys. Rev.* **1954**, *96*, 99.
[32] T. Kasuya, *Prog. Theor. Phys.* **1956**, *16*, 45.
[33] J. Kondo, *Prog. Theor. Phys.* **1964**, *32*, 37.
[34] A. C. Hewson, *The Kondo Problem to Heavy Fermions*, Cambridge University Press, London **1997**.
[35] Y. Li, S. M. Winter, D. A. S. Kaib, K. Riedl, R. Valentí, *Phys. Rev. B* **2021**, *103*, L220408.
[36] L. Savary, L. Balents, *Rep. Prog. Phys.* **2017**, *80*, 016502.
[37] B. C. Chakoumakos, D. Mandrus, *J. Alloys Compd.* **1998**, *281*, 157.
[38] C. Lv, X. Cheng, J. Sui, K. Jia, X. Dong, M. Ding, B. Pan, *Phys. B: Condens.* **2024**, *677*, 415733.
[39] V. V. Novikov, N. V. Mitroshenkov, A. V. Matovnikov, *J. Alloys Compd.* **2015**, *646*, 906.
[40] K. Feng, C. Bush, O. Oladehin, M. Lee, R. Baumbach, *Phys. Rev. B* **2024**, *109*, 014436.
[41] I. Giannakis, D. Sar, J. Friedman, C.-J. Kang, M. Janoschek, P. Das, E. D. Bauer, G. Kotliar, P. Aynajian, *Phys. Rev. Res.* **2022**, *4*, L022030.
[42] L. Krause, R. Herbst-Irmer, G. M. Sheldrick, D. Stalke, *J. Appl. Crystallogr.* **2015**, *48*, 3.
[43] G. Sheldrick, *Acta Crystallogr. A.* **2015**, *71*, 3.
[44] G. Sheldrick, *Acta Crystallogr. C.* **2015**, *71*, 3.
[45] A. Coelho, *J. Appl. Crystallogr.* **2018**, *51*, 210.
[46] G. Kresse, J. Furthmüller, *Comput. Mater. Sci* **1996**, *6*, 15.
[47] J. P. Perdew, K. Burke, M. Ernzerhof, *Phys. Rev. Lett.* **1996**, *77*, 3865.
[48] P. E. Blöchl, *Phys. Rev. B* **1994**, *50*, 17953.
[49] S. Choi, P. Semon, B. Kang, A. Kutepov, G. Kotliar, *Comput. Phys. Commun.* **2019**, *244*, 277.
[50] R. Adler, C. Melnick, G. Kotliar, *Comput. Phys. Commun.* **2024**, *294*, 108907.
[51] A. L. Kutepov, V. S. Oudovenko, G. Kotliar, *Comput. Phys. Commun.* **2017**, *219*, 407.
[52] A. L. Kutepov, *Phys. Rev. B* **2021**, *103*, 165101.
[53] C. Melnick, P. Sémon, K. Yu, N. D'Imperio, A.-M. Tremblay, G. Kotliar, *Comput. Phys. Commun.* **2021**, *267*, 108075.
[54] K. Haule, C.-H. Yee, K. Kim, *Phys. Rev. B* **2010**, *81*, 195107.

Manuscript received: February 4, 2025
Revised manuscript received: March 14, 2025
Version of record online: April 10, 2025